Research Article | Vol. 30, No. 21 / 10 Oct 2022 / Optics Express 38953
Optics EXPRESS

Plasmonic *hot-electron* reconfigurable photodetector based on phase-change material Sb_2S_3

GONZALO SANTOS,[1] MARIN GEORGHE,[2] CORNEL COBIANU,[2] MIRCEA MODREANU,[3] MARIA LOSURDO,[4] YAEL GUTIÉRREZ,[5,*] AND FERNANDO MORENO[1,6]

[1]*Group of Optics. Department of Applied Physics Faculty of Sciences, University of Cantabria, Spain*
[2]*NANOM MEMS Srl, G. Cosbuc 9, 505400 Rasnov, Brasov, Romania*
[3]*Tyndall National Institute-University College Cork, Lee Maltings, Dyke Parade, Cork T12 R5CP, Ireland*
[4]*CNR ICMATE, Corso Stati Uniti 4, I-35127, Padova, Italy*
[5]*Institute of Nanotechnology CNR-NANOTEC, Via Orabona 4, 70126 Bari, Italy*
[6]*fernando.moreno@unican.es*
[*]*yael.gutierrezvela@nanotec.cnr.it*

Abstract: Hot-carrier based photodetectors and enhanced by surface plasmons (SPs) hot-electron injection into semiconductors, are drawing significant attention. This photodetecting strategy yields to narrowband photoresponse while enabling photodetection at sub-bandgap energies of the semiconductor materials. In this work, we analyze the design of a reconfigurable photodetector based on a metal-semiconductor (MS) configuration with interdigitated dual-comb Au electrodes deposited on the semiconducting Sb_2S_3 phase-change material. The reconfigurability of the device relies on the changes of refractive index between the amorphous and crystalline phases of Sb_2S_3 that entail a modulation of the properties of the SPs generated at the dual-comb Au electrodes. An exhaustive numerical study has been realized on the Au grating parameters formed by the dual-comb electrodes, and on the SP order with the purpose of optimizing the absorption of the device, and thus, the responsivity of the photodetector. The optimized photodetector layout proposed here enables tunable narrowband photodetection from the O telecom band (λ = 1310 nm) to the C telecom band (λ = 1550 nm).

1. Introduction

Excitation of surface plasmons (SP) in metallic plasmonic nanostructures enables enhanced light-matter interactions at the nanoscale through coherent oscillations of the free-electron cloud of the metal. Surface plasmons, which have very short lifetimes (i.e. of the order of femtoseconds), can decay non radiatively generating a small but highly energetic population of non-thermal carriers above the Fermi level at the surface of the metallic structure [1,2]. These are referred as *hot-electrons*, and in recent years have gained a lot of attention in different fields spanning from photodetection [3,4] to photovoltaics [5] and photochemistry [6–9].

When metallic nanostructures are interfaced with semiconductors, *hot- electrons* can be injected into the semiconductor if their energy is enough to overcome the Schottky barrier (Φ_{SB}, i.e. energy difference between the conduction band edge of the semiconductor and the Fermi energy of the metal) and lower than the semiconductor band gap (E_g), thus, leading to photocurrents that can be detected with an external circuit. Because *hot-electrons* only need energy to meet the condition $\Phi_{SB} < h\nu < E_g$, this strategy enables photodetection well below the band edge of the semiconductor [3].

The efficiency of *hot-electrons* can be optimized by maximizing light absorption, and thus, the *hot-electron* generation, in the plasmonic nanostructures. This has led to a plethora of plasmonic

#468917 https://doi.org/10.1364/OE.468917
Journal © 2022 Received 28 Jun 2022; revised 14 Sep 2022; accepted 16 Sep 2022; published 6 Oct 2022

Optics EXPRESS

nanostructure geometries and configurations integrated in this type of photodectors spanning from periodic gratings [3,10,11], metamaterial perfect absorbers [12,13], nanoantennas [14,15] or Bragg reflectors [16,17]. Nevertheless, in all of the above *hot-electron* photodetectors, the operational photodetection bands are fixed at the fabrication step and defined by the nanostructured materials, their optical properties and those of the semiconductor.

In this work, we propose a reconfigurable photodetector based on a gold (Au) grating coupled with the phase change semiconductor antimony trisulfide (Sb_2S_3) yielding selective photodetection from the telecom O-band (λ = 1310 nm) to the telecom C-band (λ = 1550 nm). Sb_2S_3 has been recently categorized as a phase-change material (PCM) [18–20]. This type of materials can be switched between their amorphous and crystalline phases through thermal or laser irradiation stimuli while entailing a modulation in their refractive index at ultra-short times (of the order of ps) [21,22]. This capability of PCMs has already been exploited in a wide range of reconfigurable photonic platforms that expand from programmable photonics [23,24], neuromorphic computing [25], non-volatile and rewritable data storage [21,26], to tunable metasurfaces and flat optics with amplitude/phase control [27], cloaking [28], and reflective displays [29]. Therefore, in the proposed *hot-electron* photodetector configuration, the photodetection band can be tuned through the amorphous-to-crystalline phase change in the Sb_2S_3 that produces a modulation in its refractive index and, consequently, a change in the resonant frequency of the SP generated at the Au grating. Other authors have reported other design of Au-Sb_2S_3 reconfigurable *hot-electron* photodetector based on a metal–dielectric–metal (Au-Sb_2S_3-Au) cavity [30]. Trough the proposed design in this work, a narrower spectral response with more sensitivity to the incident polarization can be generated. Because the energy band gap and absorption edge of crystalline and amorphous phases of Sb_2S_3 are 1.6-1.7 eV and 2.0-2.2 eV respectively [20], Sb_2S_3 is a potential platform for reconfigurable *hot-electron* photodetection in the near-infrared and telecom bands only limited by the Schottky barrier imposed by the interfaced material of the plasmonic structures. This paper is structured as follows. Sect. 2, is devoted to the methodology of this research. In Sect. 3 the device design and working principle are developed. Sect. 4 contains how the proposed system can be optimized to get the maximum detection efficiency (responsivity). In Sect. 5, the main results of this research are presented, and finally, in Sect. 6 the main conclusions are drawn.

2. Methods

In order to couple the nanostructured metal to the semiconductor, in this research, the grating method will be chosen. Bearing this in mind, the numerical calculations performed in this research are based in two methods. The Rigorous Coupled Wave Analysis and Finite-Difference Time-Domain (FDTD) simulations. The first, consists in a semi-analytical method of computational electromagnetics that is typically employed to solve the diffraction problem of an electromagnetic field by a given periodic grating structure. The devices and fields are represented by a sum of spatial harmonics, since RCWA is a Fourier-space method. The absorbance profiles of the proposed photodetector have been obtained through this method considering a highest diffracted order of N=60.

The FDTD simulations [31] have been performed using Ansys Lumerical 2022 to obtain the distribution of the scattered electric field in near field regime. This numerical analysis technique is used for modeling computational electrodynamics (finding approximate solutions to a system of coupled differential equations by time discretization). Nonuniform mesh settings were used in these simulations. A plane wave was set as source. Periodic boundary conditions were used in the x and y directions to simulate an infinite number of the gold ribs of intinite length over Sb_2S_3.

3. Device design and working principle

A scheme of the proposed reconfigurable photodetector is represented in Fig. 1(a). It consists of a metal-semiconductor (MS) configuration with interdigitated dual-comb gold electrodes,

Optics EXPRESS

deposited on semiconducting Sb_2S_3. The effect of adding a capping layer to avoid the oxidation of the PCM, and to prevent the reshaping of the gold grating at the high temperatures required for amorphization has been modelled and discussed in Supplement 1. Additionally, the effect of the Sb_2S_3 layer thickness, its impact on the responsivity of the device, and choices for substrate material have also been discussed in the SI. The periodically arranged metal digits (ribs) represent, at the same time, a metal grating for the incident light to be coupled to the semiconductor substrate for detection. All results were simulated considering normal incidence and light polarization perpendicular to the rib direction. This polarization is required to generate a collective effect between all the ribs as well as to allow us to ignore the length of the ribs. Consequently, the study of this system has been performed under a 2D geometrical configuration. The optical constants of both phases (amorphous and crystalline) of Sb_2S_3 are represented in Fig. 1(b). The imaginary part of the refractive index for both phases is zero in the infrared regime and the real part is almost constant. The optical constants used for the simulations included in what follows are those obtained for RF sputtered films [18,19]. In general, RF sputtering provides in generally flatter surfaces (i.e., better for their use in nanolitography processes) and a higher refractive indices as compared with other deposition methods such as chemical bath deposition [20,32]. The optical constants of gold used for simulations have been obtained from Palik [33].

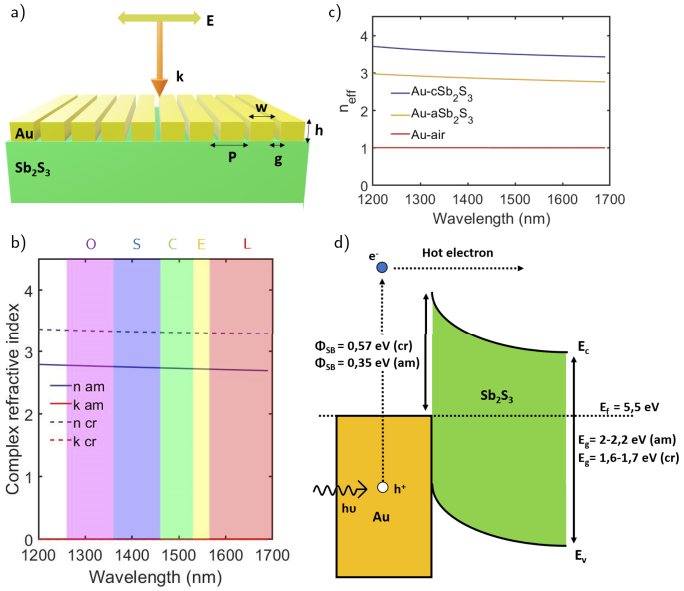

Fig. 1. (a) Scheme of the proposed reconfigurable photodetector. (b) Optical constants of Sb_2S_3 for both phases (crystalline and amorphous) in the different telecom bands. (c) Effective refractive index of the surface plasmons at the different interfaces: Au/c-Sb_2S_3 (blue), Au/a-Sb_2S_3 (yellow) and Au-Air (red) as given by Eq. (2). (d) Scheme of the *hot-electron* generation crossing the Shottky barrier (ϕ_{SB}) barrier into the conduction band of Sb_2S_3.E_c, E_v, E_f and E_g, refers to the energies of the conduction band, the valence band, the Fermi level and the band-gap of the semiconductor, respectively

The grating integrated in the designed photodetector is characterized by the following parameters: the width (w) and thickness (h) of the rib as well as the gap between two consecutive ribs (g). The periodicity (P) of the grating is $P = w + g$. For these systems, the real part of the dielectric function of both the metal (Au, ϵ_1) and the dielectric medium (in this case, air or Sb_2S_3,

Optics EXPRESS

ϵ_2), the resonant wavelength (λ), and the incident angle (θ) are related as [34]

$$\lambda = \frac{P}{m}(\pm\sqrt{\frac{\epsilon_1\epsilon_2}{\epsilon_1+\epsilon_2}} - \epsilon_1 sin(\theta)) \tag{1}$$

$$n_{eff} = \sqrt{\frac{\epsilon_1\epsilon_2}{\epsilon_1+\epsilon_2}} \tag{2}$$

In Eq. (1), the square root containing the metal dielectric function and that of the dielectric medium can be understood as an effective refractive index (n_{eff}) of the surface plasmon (Eq. (2)). By considering all the possible interfaces, the n_{eff} of the SP is represented in Fig. 1(c). The surface plasmon can be generated at two different interfaces either air-Au or Au-Sb_2S_3 (crystalline and amorphous). For photodetection, we will focus on the latter, where *hot-electrons* generated by the SP non-radiative decay with energy lower than the bandgap (2.0-2.2 eV for the amorphous and 1.6-1.7 eV for the crystalline [20]) and energy higher than the Schottky barrier (Φ_{SB}) are transferred into the conduction band of Sb_2S_3. *Hot-electrons* surmounting this barrier and entering the conduction band of Sb_2S_3, are carried by the electric field from the interface to the positive electrode of the biased photodetector and then to the external circuit, creating the SP enhanced photocurrent. The Schottky barrier is different for the amorphous ad crystalline phases of Sb_2S_3. In literature, there is a high dispersion in the values of the Schottky barrier between Au and Sb_2S_3, which for the latter exists a dependence on its crystalline or amorphous phase. This barrier may depend on the method used for the deposition of the Sb_2S_3 (chemical vapor deposition (CVD), atomic layer deposition (ALD), sputtering, chemical bath deposition (CBD), ...) and the surface termination of the layers. In this work, the chosen values of the Schottky barrier are 0.35 eV [35] and 0.57 eV [30] for the amorphous and crystalline geometries respectively. A scheme for *hot-electron* generation due to SP decay is represented in Fig. 1(d). The internal quantum efficiency (η) of the transfer of *hot-electrons* from the Au to the Sb_2S_3 can be estimated through Fowler's model [36], which already has been proven to accurately predict the quantum efficiency in a series of *hot-electron* photodetectors [3,11,12,37]. Within this model, the quantum efficiency depends on the Schottky barrier, the Fermi energy (E_F) of the metal and the energy of incident photons ($h\nu$) and is given by Eq. (3). Here, the Fermi energy of the metallic gold has been taken as E_F = 5.5 eV [38]. The quantum efficiency of the device for both Sb_2S_3 phases is shown in the SI. The responsivity (R) is a measure of optical-to-electrical conversion efficiency of a photodetector and it is usually expressed by the value of the photocurrent (mA) generated by each milliwatt (mW) of optical signal and follows Eq. (4). It is directly proportional to the absorbance (A) generated by the *hot-electron* transition. Therefore, for the optimization of the device, its absorbance should be as high as possible to guarantee maximum photoresponsivity.

$$\eta = \frac{(h\nu - \phi_{SB})^2}{8E_F h\nu} \tag{3}$$

$$R = \frac{A\eta q}{h\nu} \tag{4}$$

4. Optimization

For normal incidence and polarization perpendicular to the ribs and normal incidence, the grating parameters should be optimized to generate the maximum absorption at the desired resonant wavelength and consequently, the responsivity R of the photodetector, according to Eq. (4).

The first step is determining the wavelength of interest (WOI) for the surface plasmon generation. In this study, as WOI we have chosen 1550 nm (C-band) as it is the most common operating wavelength in integrated photonics. The period P (Eq. (1)) required for this WOI, and considering Sb_2S_3 in its crystalline phase, can be calculated by using the effective refractive index n_{eff} of the surface plasmon (see Fig. 1(c)) for different diffraction orders (m). The absorbance profile

Optics EXPRESS

is studied for the first three diffraction orders (m = 1, m = 2 and m = 3). For the WOI = 1550 nm, as the diffracted order is increased, a higher period of the grating is needed, and thus, the complexity in the fabrication of the device is reduced. The corresponding periods are: P_1 = 446 nm, P_2 = 892 nm and P_3 = 1338 nm. Keeping these parameters, and considering the Au/a-Sb_2S_3 system, the WOI shifted to 1300 nm (O-band) because of the lower refractive index of the amorphous phase of Sb_2S_3 as compared with the crystalline one. The parameters resulting from these calculations are summarized in Tables 1 and 2. It is important to highlight the importance of the transition between the O band and the C band and its technological relevance. Oldest devices usually work in the O-band while currently, most of the optical circuits work in the C band. Therefore, this detector can be a nexus to join modern and old devices.

Table 1. Grating periods calculated using Eq. (1), for a resonant wavelength of 1550 nm in the Au/c-Sb_2S_3 interface and for the first three diffracted orders.

Order	m=1	m=2	m=3
Period (nm)	446	892	1338

Table 2. Resonant wavelength (λ_{SP}) of the surface plasmons associated to the periods shown in the Table 1 for both amorphous and crystalline phases of Sb_2S_3.

Phase	Amorphous	Crystalline
λ_{SP} (nm)	1300 (O-band)	1550 (C-band)

The gap (g) and the thicknesses (h) of the ribs cannot be calculated from Eq. (1) because this relation is deduced for smooth metallic gratings [34]. It should be noted that reducing the gap between the ribs, their interaction is stronger leading to a higher absorbance. Therefore, the gap value has been fixed to 30 nm, a feature affordable size for different nanolithography techniques [39].

The optimization of the thickness h for both phases (amorphous - λ_{SP}=1300 nm and crystalline - λ_{SP}=1550 nm) and for the three different periods related to the three diffraction orders considered here, are represented in Fig. 2. The thickness h is varied from 170 nm to 270 nm in order to find the optimum value with higher absorbance. In each case, the optimum thickness is different. For each period, the thickness of the ribs has been chosen as the average between the those thicknesses that gives the higher absorbance for the crystalline and amorphous phases. In Fig. 2(e), there is no absorbance peak. This issue will be discussed in the next section. The values for the optimized thicknesses are summarized in Table 3.

Table 3. Optimized thicknesses values of *h* for the three calculated periods and for both phases. As the optimum thickness is different for each period, this is taken as the average between the ideal thickness for the amorphous and crystalline phases. As a reminder, the resonant wavelengths (λ_{SP}) are around 1300 nm and 1550 nm for the amorphous and crystalline phases respectively.

Period (nm)	$h_{amorphous}$ (nm)	$h_{crystalline}$ (nm)	$h_{optmized}$ (nm)
446	210	250	230
892	200	250	225
1338	-	240	240

Optics EXPRESS

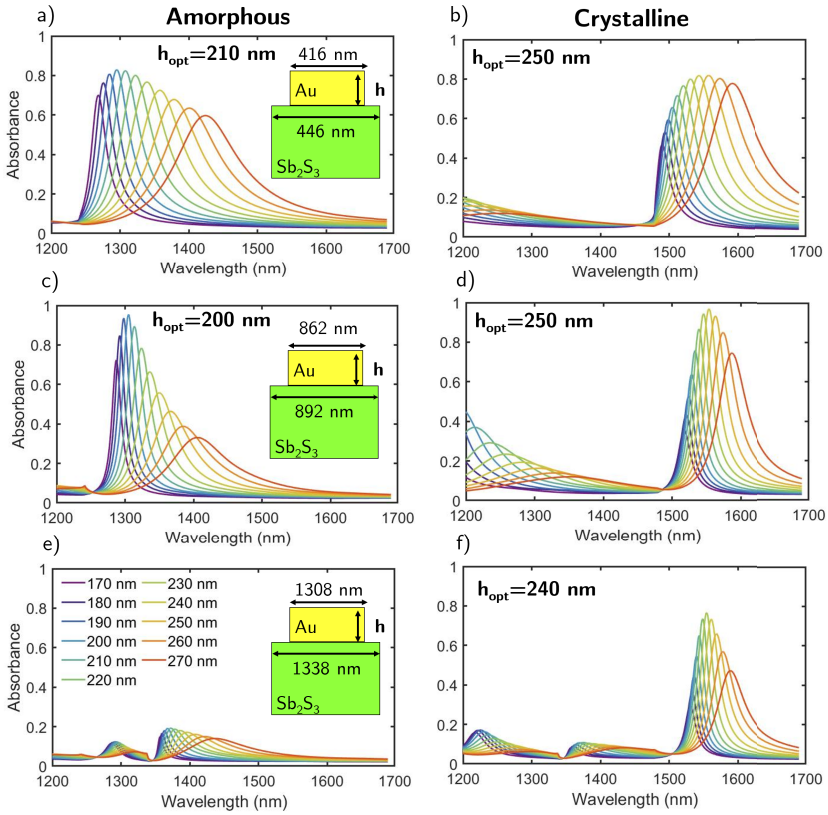

Fig. 2. Spectral absorption profile for amorphous Sb_2S_3 and the (a) first, (c) second and (e) third diffracted order respectively, and different thicknesses of the ribs (ranging from 170 nm to 270 nm). Spectral absorption profile for crystalline Sb_2S_3 and the (b) first, (d) second and (f) third diffracted order respectively and, different thicknesses of the ribs (ranging from 170 nm to 270 nm). Insets: Scheme of the unit cell for the (a) first, (d) second and (g) third diffracted order respectively.

5. Results

5.1. Normal Incidence

Once the grating parameters have been optimized, the distribution of the scattered field in the near field regime, the different absorbance spectra and, consequently, the responsivity spectral profiles are presented and discussed in this section.

The final optimized absorbance spectra for both amorphous and crystalline phases of Sb_2S_3 as well as for the three different diffracted orders are represented in Figs. 3(b), (e) and (h) respectively. The width of the absorbance peaks becomes narrower as the diffracted order is increased. The resonant wavelengths are close to 1300 nm (O-band) and 1550 nm (C-band) for the amorphous and crystalline phases of the Sb_2S_3, as it was shown in Table 2. Nevertheless, they are slightly shifted as these wavelengths were calculated using Eq. (1) in which the gap and thickness dependence is not considered. Specifically, for amorphous Sb_2S_3, when increasing diffraction order, the maximum absorbance is produced at 1339, 1324 and 1386 nm, respectively. For the crystalline phase, the maximum absorbance is produced at 1531, 1539 and 1555 nm, respectively.

Optics EXPRESS

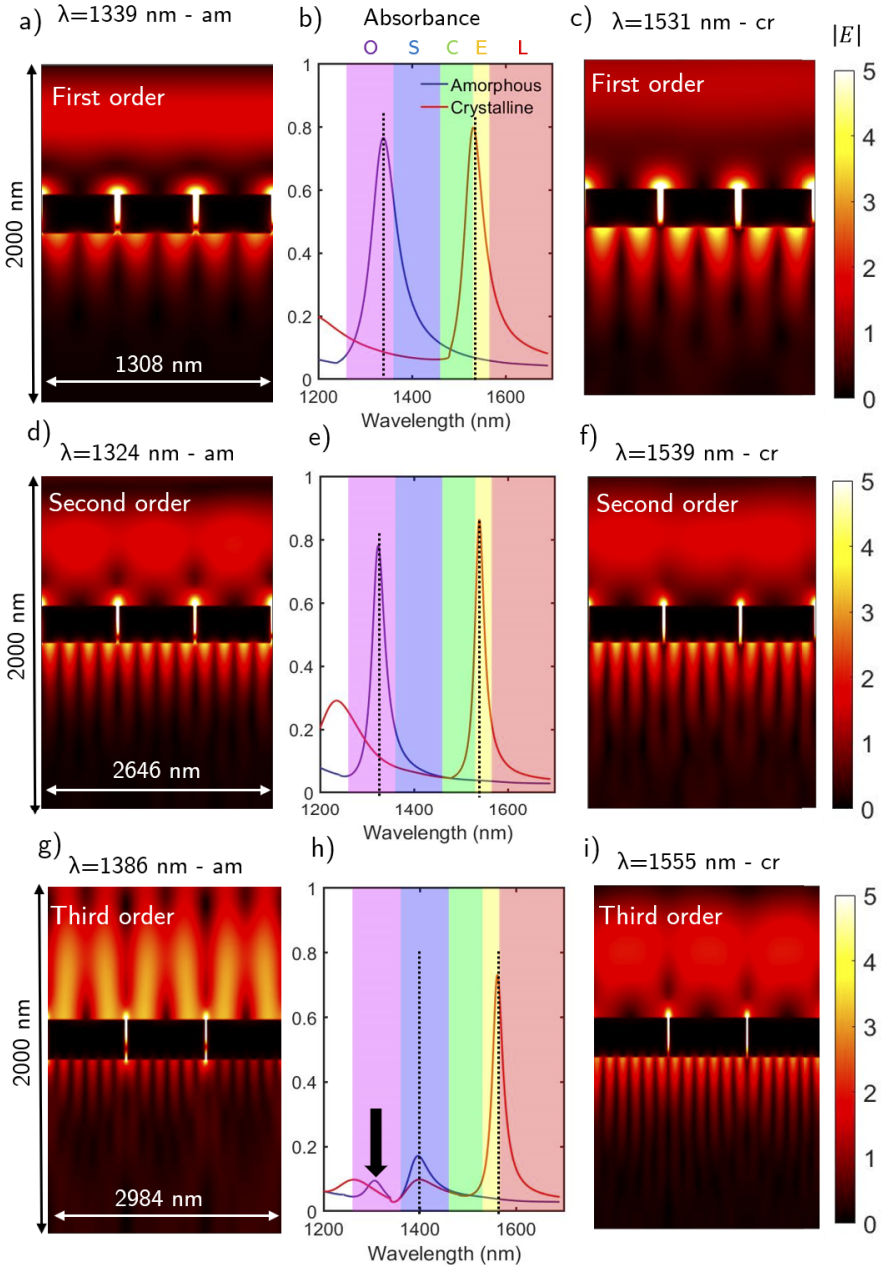

Fig. 3. Center: Absorbance spectra for the amorphous (blue) and crystalline (red) Sb_2S_3 phases, and for the (b) first, (e) second and (h) third diffraction orders. Left: Distribution of the modulus of the near electric field for the amorphous Sb_2S_3 phase resonant wavelengths s (indicated by the vertical dotted lines in the absorbance spectra) considering the (a) first, (b) second and (g) third diffraction orders. Right: Distribution of the modulus of the near electric field for the crystalline Sb_2S_3 phase resonant wavelength for the (c) first, (f) second and (i) third diffraction orders. The resonant wavelength corresponding to the third order Au-amorphous Sb_2S_3 is the one pointed out with a black arrow (λ=1310 nm).

Optics EXPRESS

The near field ($|E|$) maps for the corresponding resonant wavelengths are shown in Fig. 3. Each row corresponds to a different period (or diffraction order) and each column corresponds to each phase of the Sb_2S_3 substrate (amorphous – left column and crystalline - right column). The near-field distribution for the optimized grating by considering the first diffraction order (Figs. 3(a) and 3(c)) shows two hot spots in each rib at the Au-Sb_2S_3 interface that represents the excitation of the SP. In the case of the optimized grating by considering the second diffraction order, the near-field maps (Figs. 3(d) and 3(f)) are characterized by the presence of 4 hot spots under each rib. For the third diffraction order, the near-field plots (Figs. 3(g) and 3(i)) show 6 hot spots in each unit cell at Au-Sb_2S_3 interface. Interestingly, for the latter case, in the amorphous Sb_2S_3 case (Fig. 3(g)), no high absorbance peak is produced and two hot spots in each unit rib are generated at the air-Au interface. This phenomenon is produced because the surface plasmon is created at the Air-Au interface for this resonant wavelength (λ=1386 nm). The explanation can be understood considering Eq. (1) and the effective refractive index of the surface plasmon generated at the air-Au interface (Fig. 1(c)). As the effective refractive index of the air-Au SP is close to 1 for the first order, the resonant wavelength for this plasmon is very similar to the period. In this case, the period is 1338 nm and the resonant wavelength is 1386 nm, therefore, the first order air-Au SP can be created under these conditions. The resonant wavelength corresponding to the third order Au-amorphous Sb_2S_3 is the one pointed out with a black arrow (λ=1310 nm). As this resonant wavelength is very close to that of the air-Au SP too, energy absorption is split between the two interfaces. Thus, as much of the incident light with wavelength about 1300 nm is simultaneously resonantly absorbed at the first interface (air-Au) and at the interface between Au and a-Sb_2S_3, leading to the quenched peak shown in Fig. 2(e). From the experimental point of view, phase change materials not only present pure amorphous and crystalline phases. A mix of both can be controllably induced in the PCM film as already demonstrated for GST [26,40]. The effective refractive index of these samples can be estimated through a Bruggeman model [41] by considering the optical properties of both phases.

The absorbance spectra for these intermediate phases, and the first three diffracted orders studied previously, are shown in Figs. 4(b), (e) and (h) respectively. These intermediate states have been simulated by varying the volume percentage for each phase present in the sample. The percentages considered for these simulations have been 25% 50% and 75% to work in a range where the Bruggeman effective medium approximation holds. Depending on the crystallinity of the Sb_2S_3, the absorbance profile can be tuned from the O to the C-band, and vice versa, covering most of the telecom bands.

The responsivity profile can be obtained from the absorbance spectra as it was shown in Eqs. (3) and (4) by considering the Fermi energy of gold and the Schottky barrier between metal and semiconductor. The Schottky barrier of these intermediates states is expected to be between 0.35 eV (amorphous) and 0.57 eV (crystalline). As the Schottky barrier is unknown for all of these intermediates states, in these calculations it has been considered the value of the Schottky barrier of the c-Sb_2S_3 for all of these mix phases (the most unfavorable case). The responsivity decreases as the Schottky barrier increases. The resulting responsivity for all of these phases and for the different three diffracted orders is shown in Figs. 4(c), (f) and (i), respectively. For comparison, the maximum and the full width at half maximum (FWHM) of the responsivity peaks for the three different diffracted orders as a function of the crystallinity of the Sb_2S_3 substrate (amorphous - 0%, crystalline - 100% and intermediate states - 25%, 50% and 75%) are represented in Figs. 4(g) and 4(f) respectively. The highest responsivity maximum and the lower FWHM of the responsivity curves are generated by the SP of second order (m = 2).

5.2. Angular dependence

All the simulations in the previous sections have been performed under normal incidence illumination. Nevertheless, under realistic illuminating conditions of a photodetecting device,

Optics EXPRESS

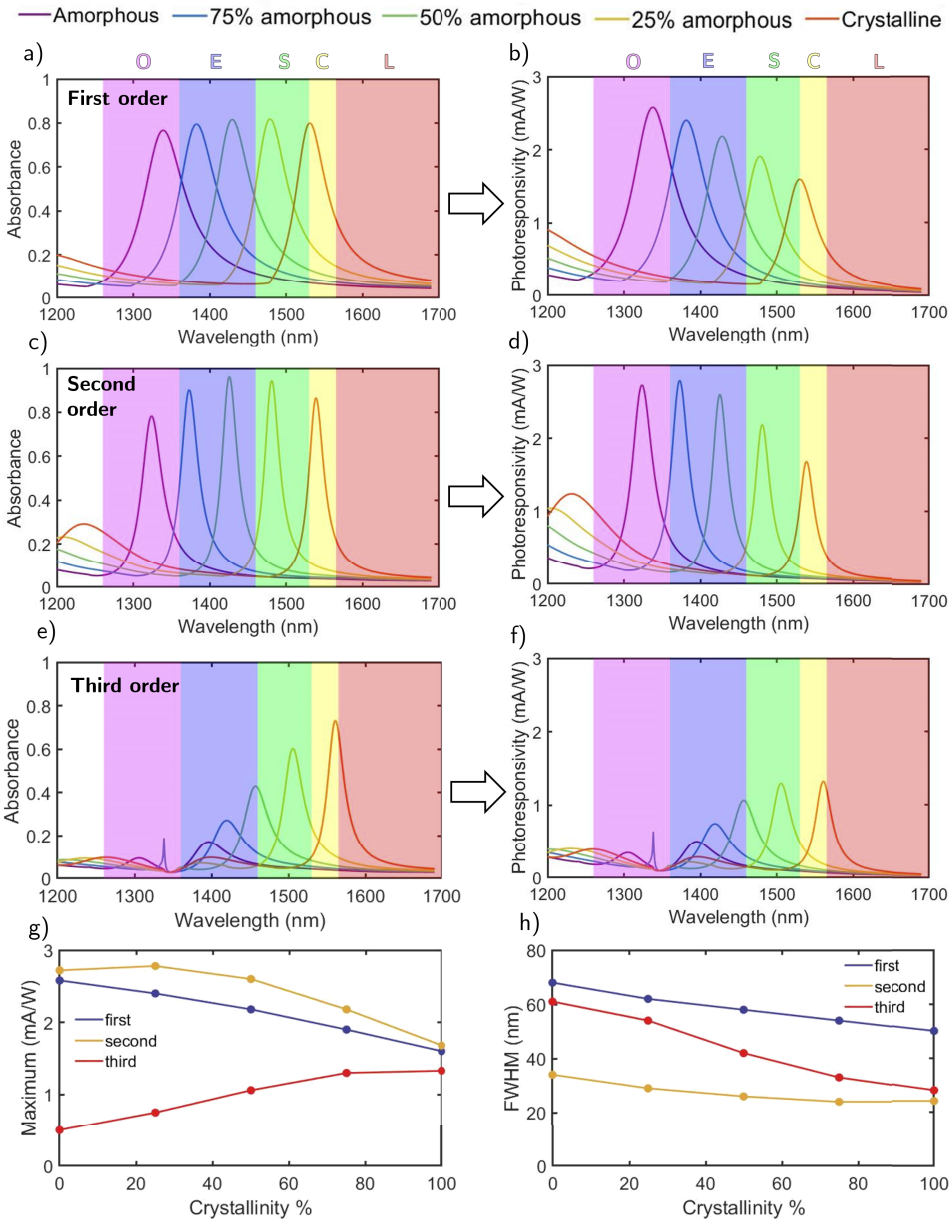

Fig. 4. Absorbance spectral profiles of amorphous, crystalline and intermediate phases of Sb_2S_3 for the (a) first, (c) second and (e) third diffracted order. Responsivity spectra for all the studied phases of Sb_2S_3 for the (b) first, (d) second and (f) third diffracted order. (g) Maximum and (h) full width at half maximum (FWHM)of responsivity peaks for the three different orders as a function of the crystallinity of Sb_2S_3 (amorphous - 0%, crystalline - 100% and intermediate states - 25%, 50% and 75%).

Optics EXPRESS

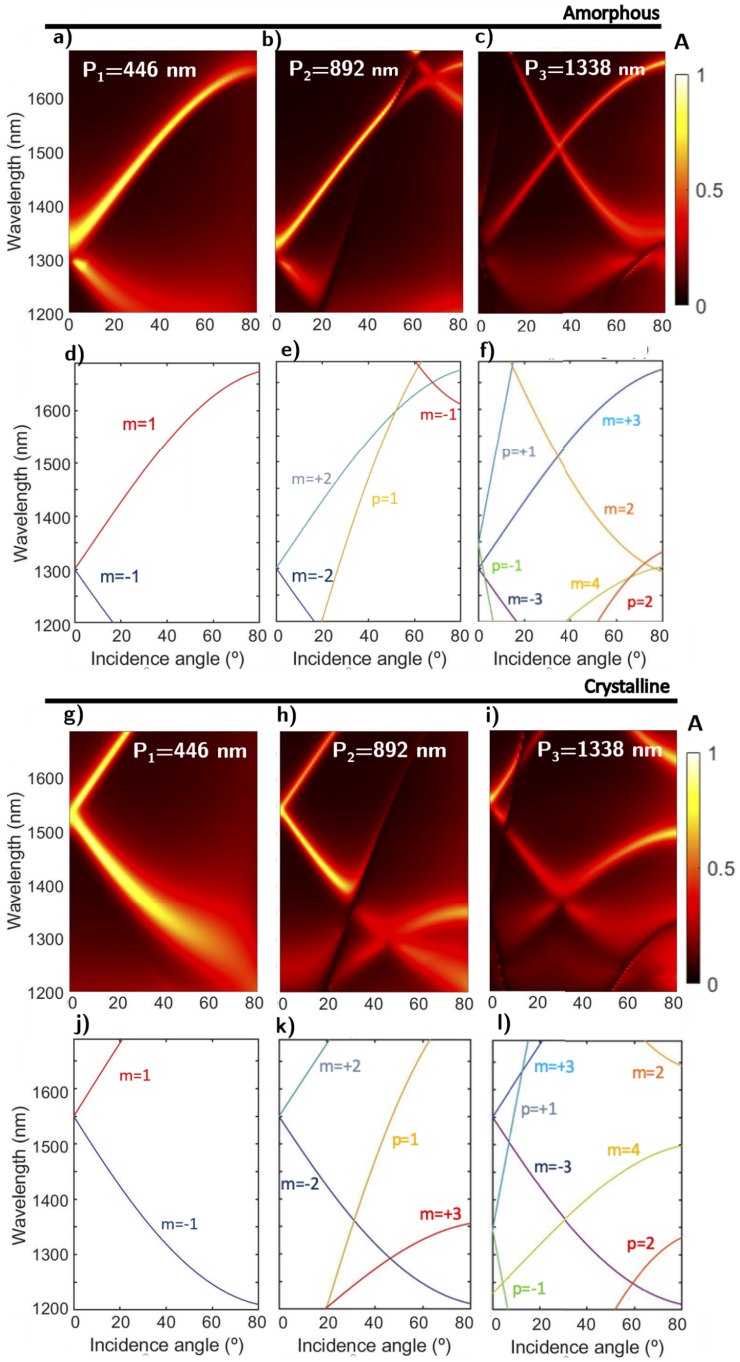

Fig. 5. (a-c) Absorbance spectra for the amorphous phase of the illuminating beam incident angle by considering the three diffracted orders, respectively. (g-i) Absorbance spectra for the crystalline phase as a function of the illuminating beam incident angle by considering the three diffracted orders respectively. (d-f) Resonant wavelength position as a function of the illuminating beam incident angle and given by Eq. (1) for the amorphous phase. (j-l) Resonant wavelength position as a function of the illuminating beam incident angle and given by Eq. (1) for the crystalline phase.

Optics EXPRESS

it is reasonable to consider also light illumination at non-normal incident angles. For the geometry proposed here, the absorbance spectra shows angular dependence, and consequently, the responsivity shows differences for every angle of incidence of the illuminating beam. In order to assess the importance of this issue, the absorbance as a function of the wavelength and the angle of incidence is represented in Fig. 5. The absorbance colormaps are represented along with the the analytical solution from Eq. (1). The indices labeling the curves in the analytical solution (i.e. m and p) indicates the diffraction order of the SP generated at the Au-Sb_2S_3 interface (m) and at the Air-Au interface (p). A good agreement between numerical simulation and analytical calculations is obtained.

6. Conclusions

A reconfigurable photodetector consisting of Au ribs (i.e. interdigitated dual-comb Au electrodes) on a phase-change material Sb_2S_3 substrate operating at the different telecom bands and based on the non-radiative decay of SP (hot electrons) generated at the interface Sb_2S_3 has been designed. The tunability of the device is provided through the amorphous to crystalline transition of the Sb_2S_3 layer. For crystalline Sb_2S_3 the responsivity of the photodetector is maximum at the telecom C-band ($\lambda = 1550$ nm), while for amorphous Sb_2S_3 the responsivity peaks at the telecom O-band ($\lambda = 1310$ nm). The device has been optimized for three different surface plasmon diffraction orders while concluding that the second order gives the highest and narrowest band responsitivity of the photodetector for normal incidence illumination. For non-normal incidence, extra peaks in the absorption profiles can be observed due to the angular dependence of surface plasmon. This effect is amplified when considering higher surface plasmon diffraction orders.

Funding. Horizon 2020 Framework Programme (No 899598 – PHEMTRONICS).

Disclosures. The authors declare no conflict of interest.

Data availability. Data underlying the results presented in this paper are not publicly available at this time but may be obtained from the authors upon reasonable request.

Supplemental document. See Supplement 1 for supporting content.

References

1. A. O. Govorov, H. Zhang, H. V. Demir, and Y. K. Gun'Ko, "Photogeneration of hot plasmonic electrons with metal nanocrystals: Quantum description and potential applications," Nano Today **9**(1), 85–101 (2014).
2. L. V. Besteiro, P. Yu, Z. Wang, A. W. Holleitner, G. V. Hartland, G. P. Wiederrecht, and A. O. Govorov, "The fast and the furious: Ultrafast hot electrons in plasmonic metastructures. Size and structure matter," Nano Today **27**, 120–145 (2019).
3. A. Sobhani, M. W. Knight, Y. Wang, B. Zheng, N. S. King, L. V. Brown, Z. Fang, P. Nordlander, and N. J. Halas, "Narrowband photodetection in the near-infrared with a plasmon-induced hot electron device," Nat. Commun. **4**(1), 1643 (2013).
4. K.-T. Lin, H. Lin, and B. Jia, "Plasmonic nanostructures in photodetection, energy conversion and beyond," Nanophotonics **9**(10), 3135–3163 (2020).
5. C. Clavero, "Plasmon-induced hot-electron generation at nanoparticle/metal-oxide interfaces for photovoltaic and photocatalytic devices," Nat. Photonics **8**(2), 95–103 (2014).
6. M. J. Kale, T. Avanesian, and P. Christopher, "Direct photocatalysis by plasmonic nanostructures," ACS Catal. **4**(1), 116–128 (2014).
7. X. Zhang, X. Li, M. E. Reish, D. Zhang, N. Q. Su, Y. Gutiérrez, F. Moreno, W. Yang, H. O. Everitt, and J. Liu, "Plasmon-Enhanced Catalysis: Distinguishing Thermal and Nonthermal Effects," Nano Lett. **18**(3), 1714–1723 (2018).
8. W. Hou and S. B. Cronin, "A review of surface plasmon resonance-enhanced photocatalysis," Adv. Funct. Mater. **23**(13), 1612–1619 (2013).
9. S. Linic, U. Aslam, C. Boerigter, and M. Morabito, "Photochemical transformations on plasmonic metal nanoparticles," Nat. Mater. **14**(6), 567–576 (2015).
10. H. Chalabi, D. Schoen, and M. L. Brongersma, "Hot-Electron Photodetection with a Plasmonic Nanostripe Antenna," Nano Lett. **14**(3), 1374–1380 (2014).
11. W. Wang, L. V. Besteiro, P. Yu, F. Lin, A. O. Govorov, H. Xu, and Z. Wang, "Plasmonic hot-electron photodetection with quasi-bound states in the continuum and guided resonances," Nanophotonics **10**(7), 1911–1921 (2021).

Optics EXPRESS

12. W. Li and J. Valentine, "Metamaterial Perfect Absorber Based Hot Electron Photodetection," Nano Lett. **14**(6), 3510–3514 (2014).
13. Y. Zhu, P. Yu, E. Ashalley, T. Liu, F. Lin, H. Ji, J. Takahara, A. Govorov, and Z. Wang, "Planar hot-electron photodetector utilizing high refractive index MoS_2 in Fabry–Pérot perfect absorber," Nanotechnology **31**(27), 274001 (2020).
14. M. W. Knight, H. Sobhani, P. Nordlander, and N. J. Halas, "Photodetection with Active Optical Antennas," Science **332**(6030), 702–704 (2011).
15. K.-T. Lin, H.-L. Chen, Y.-S. Lai, and C.-C. Yu, "Silicon-based broadband antenna for high responsivity and polarization-insensitive photodetection at telecommunication wavelengths," Nat. Commun. **5**(1), 3288 (2014).
16. C. Zhang, K. Wu, V. Giannini, and X. Li, "Planar Hot-Electron Photodetection with Tamm Plasmons," ACS Nano **11**(2), 1719–1727 (2017).
17. J. Wang, Y. Zhu, W. Wang, Y. Li, R. Gao, P. Yu, H. Xu, and Z. Wang, "Broadband Tamm plasmon-enhanced planar hot-electron photodetector," Nanoscale **12**(47), 23945–23952 (2020).
18. W. Dong, H. Liu, J. K. Behera, L. Lu, R. J. H. Ng, K. V. Sreekanth, X. Zhou, J. K. W. Yang, and R. E. Simpson, "Wide bandgap phase change material tuned visible photonics," Adv. Funct. Mater. **29**(6), 1806181 (2019).
19. M. Delaney, I. Zeimpekis, D. Lawson, D. W. Hewak, and O. L. Muskens, "A New Family of Ultralow Loss Reversible Phase-Change Materials for Photonic Integrated Circuits: Sb_2S_3 and Sb_2Se_3," Adv. Funct. Mater. **30**(36), 2002447 (2020).
20. Y. Gutierrez, A. P. Ovvyan, G. Santos, D. Juan, S. A. Rosales, J. Junquera, P. García-Fernández, S. Dicorato, M. Giangregorio, E. Dilonardo, F. Palumbo, M. Modreanu, J. Resl, O. Ischenko, G. Garry, T. Jouzi, M. Gheorghe, C. Cobianu, K. Hingerl, C. Cobet, F. Moreno, W. H. Pernice, and M. Losurdo, "Interlaboratory Study on Sb_2S_3 Interplay between Structure, Dielectric Function and Amorphous-to-Crystalline Phase Change for Photonics," iScience **25**(6), 104377 (2022).
21. M. Wuttig and N. Yamada, "Phase-change materials for rewriteable data storage," Nat. Mater. **6**(11), 824–832 (2007).
22. M. Wuttig, H. Bhaskaran, and T. Taubner, "Phase-change materials for non-volatile photonic applications," Nat. Photonics **11**(8), 465–476 (2017).
23. M. Stegmaier, C. Ríos, H. Bhaskaran, C. D. Wright, and W. H. P. Pernice, "Nonvolatile All-Optical 1×2 Switch for Chipscale Photonic Networks," Adv. Opt. Mater. **5**(1), 1600346 (2017).
24. M. Delaney, I. Zeimpekis, H. Du, X. Yan, M. Banakar, D. J. Thomson, D. W. Hewak, and O. L. Muskens, "Nonvolatile programmable silicon photonics using an ultralow-loss Sb_2Se_3 phase change material," Sci. Adv. **7**(25), 1 (2021).
25. J. Feldmann, N. Youngblood, C. D. Wright, H. Bhaskaran, and W. H. P. Pernice, "All-optical spiking neurosynaptic networks with self-learning capabilities," Nature **569**(7755), 208–214 (2019).
26. C. Ríos, M. Stegmaier, P. Hosseini, D. Wang, T. Scherer, C. D. Wright, H. Bhaskaran, and W. H. P. Pernice, "Integrated all-photonic non-volatile multi-level memory," Nat. Photonics **9**(11), 725–732 (2015).
27. S. Abdollahramezani, O. Hemmatyar, H. Taghinejad, A. Krasnok, Y. Kiarashinejad, M. Zandehshahvar, A. Alu, and A. Adibi, "Tunable nanophotonics enabled by chalcogenide phase-change materials," Nanophotonics **9**(5), 1189–1241 (2020).
28. S. Lepeshov, A. Krasnok, and A. Alù, "Nonscattering-to-Superscattering Switch with Phase-Change Materials," ACS Photonics **6**(8), 2126–2132 (2019).
29. S. G. C. Carrillo, L. Trimby, Y. Y. Au, V. K. Nagareddy, G. Rodriguez-Hernandez, P. Hosseini, C. Ríos, H. Bhaskaran, and C. D. Wright, "A Nonvolatile Phase-Change Metamaterial Color Display," Adv. Opt. Mater. **7**(18), 1801782 (2019).
30. S. K. Chamoli, G. Verma, S. C. Singh, and C. Guo, "Phase change material based hot electron photodetection," Nanoscale **13**(2), 1311–1317 (2021).
31. D. M. Sullivan, *Electromagnetic simulation using the FDTD method* (John Wiley & Sons, 2013).
32. Y. Gutierrez, A. Fernández, S. Rosales, C. Cobianu, M. Gheorghe, M. Modreanu, J. Saiz, F. Moreno, and M. Losurdo, "Polarimetry Analysis and Optical Contrast of Sb_2S_3 Phase Change Material," Opt. Mater. Express **12**(4), 1531 (2022).
33. E. D. Palik, *Handbook of optical constants of solids*, vol. 3 (Academic press, 1998).
34. H. Raether, *Surface Plasmons on Smooth and Rough Surfaces and on Gratings*, vol. 111 of *Springer Tracts in Modern Physics* (Springer Berlin Heidelberg, Berlin, Heidelberg, 1988).
35. O. Savadogo and K. C. Mandal, "Low Cost Schottky Barrier Solar Cells Fabricated on CdSe and Sb_2S_3 Films Chemically Deposited with Silicotungstic Acid," J. Electrochem. Soc. **141**(10), 2871–2877 (1994).
36. R. H. Fowler, "The Analysis of Photoelectric Sensitivity Curves for Clean Metals at Various Temperatures," Phys. Rev. **38**(1), 45–56 (1931).
37. Y. K. Lee, C. H. Jung, J. Park, H. Seo, G. A. Somorjai, and J. Y. Park, "Surface Plasmon-Driven Hot Electron Flow Probed with Metal-Semiconductor Nanodiodes," Nano Lett. **11**(10), 4251–4255 (2011).
38. N. W. Ashcroft and N. D. Mermin, *Solid State Physics* (Brooks/Cole, 1976), 2nd ed.
39. A. Pimpin and W. Srituravanich, "Review on micro-and nanolithography techniques and their applications," Eng. J. **16**(1), 37–56 (2012).
40. S. Cueff, A. Taute, A. Bourgade, J. Lumeau, S. Monfray, Q. Song, P. Genevet, B. Devif, X. Letartre, and L. Berguiga, "Reconfigurable Flat Optics with Programmable Reflection Amplitude Using Lithography-Free Phase-Change Material Ultra-Thin Films (Advanced Optical Materials 2/2021)," Adv. Opt. Mater. **9**(2), 2170006 (2021).

Optics EXPRESS

41. D. A. G. Bruggeman, "Berechnung verschiedener physikalischer Konstanten von heterogenen Substanzen. I. Dielektrizitätskonstanten und Leitfähigkeiten der Mischkörper aus isotropen Substanzen," Ann. Phys. **416**(7), 636–664 (1935).